Formin-mediated actin polymerization at cell–cell junctions stabilizes E-cadherin and maintains monolayer integrity during wound repair

Megha Vaman Rao[a] and Ronen Zaidel-Bar[a,b,*]
[a]Mechanobiology Institute, National University of Singapore, Singapore 117411; [b]Department of Biomedical Engineering, National University of Singapore, Singapore 117575

ABSTRACT **Cadherin-mediated cell–cell adhesion is required for epithelial tissue integrity in homeostasis, during development, and in tissue repair. E-cadherin stability depends on F-actin, but the mechanisms regulating actin polymerization at cell–cell junctions remain poorly understood. Here we investigated a role for formin-mediated actin polymerization at cell–cell junctions. We identify mDia1 and Fmnl3 as major factors enhancing actin polymerization and stabilizing E-cadherin at epithelial junctions. Fmnl3 localizes to adherens junctions downstream of Src and Cdc42 and its depletion leads to a reduction in F-actin and E-cadherin at junctions and a weakening of cell–cell adhesion. Of importance, *Fmnl3* expression is upregulated and junctional localization increases during collective cell migration. Depletion of Fmnl3 or mDia1 in migrating monolayers results in dissociation of leader cells and impaired wound repair. In summary, our results show that formin activity at epithelial cell–cell junctions is important for adhesion and the maintenance of epithelial cohesion during dynamic processes, such as wound repair.**

Monitoring Editor
Jeffrey D. Hardin
University of Wisconsin

Received: Jun 16, 2016
Revised: Jul 12, 2016
Accepted: Jul 12, 2016

INTRODUCTION

Cell-to-cell adhesion, a characteristic feature of an epithelium, is facilitated by the transmembrane calcium-dependent epithelial-cadherin (E-cadherin) receptor (van Roy and Berx, 2008). Clusters of E-cadherin receptors are organized into structures called adherens junctions (AJs; Harris and Tepass, 2010), where the extracellular domains of E-cadherin engage in *cis* and *trans* interactions to promote cell–cell adhesion (Harrison *et al.*, 2011). In addition, links between the cytoplasmic tails of E-cadherin and the actomyosin cytoskeleton are vital for the stability of cadherin clusters (Hong *et al.*, 2013) and confer on the AJ force-sensing and force-generation capabilities that allow it to participate in the complex tissue rearrangements underlying morphogenesis and wound repair (Collinet and Lecuit, 2013). At the diffraction-limited light microscopy level, the AJ can be spatially segregated into an apical densely packed band of cadherin termed the zonula adherens (ZA), and sparsely distributed clusters along the lateral membranes called lateral junctions (Takeichi, 2014; Wu *et al.*, 2014). More recently, superresolution microscopy analysis revealed that the ZA and lateral junctions comprise qualitatively and quantitatively similar E-cadherin clusters, except for increased spacing between clusters at the lateral junctions (Wu *et al.*, 2015). Moreover, at nanoscale resolution, F-actin was found to "fence" and delimit cadherin clusters, and bundles of F-actin were also evident at the apical ZA (Wu *et al.*, 2015).

Given the close association between E-cadherin receptors and the actomyosin cytoskeleton, it is not surprising that the AJ is a major hub for the activity of actin nucleators, nucleation-promoting factors (NPFs), and their regulators, such as Rho GTPases, kinases, and phosphatases (Zaidel-Bar, 2013; Guo *et al.*, 2014; Van Itallie *et al.*, 2014). By far the best-studied nucleator that is involved in regulation of actin assembly at the AJ is the Arp2/3 complex. The Arp2/3

This article was published online ahead of print in MBoC in Press (http://www.molbiolcell.org/cgi/doi/10.1091/mbc.E16-06-0429) on July 20, 2016.

The authors declare that they have no conflict of interest.

R.Z.B. conceived the project; M.V.R. designed and performed experiments; M.V.R. and R.Z.B. analyzed data and wrote the article.

*Address correspondence to: Ronen Zaidel-Bar (biezbr@nus.edu.sg).

Abbreviations used: AJ, adherens junction; 3D, three dimensional; DAD, Diaphanous autoregulatory domain; DID, Diaphanous inhibitory domain; E-cadherin, epithelial cadherin; EGFP, enhanced green fluorescent protein; EGTA, ethylene glycol-bis(β-aminoethyl ether)-*N*,*N*,*N*′,*N*′-tetraacetic acid; FH2, formin homology 2; FMNL, formin like; FRAP, fluorescence recovery after photobleaching; KD, knockdown; NPF, nucleation-promoting factors; RT-PCR, reverse transcription PCR; siRNA, small interfering RNA; SMIFH2, small molecule inhibitor of FH2; ZA, zonula adherens.

complex localizes to the AJ and coimmunoprecipitates with E-cadherin, and inhibition of Arp2/3 severely affects cell–cell junction formation and steady-state F-actin turnover at a mature AJ (Verma *et al.*, 2004, 2012; Kovacs *et al.*, 2011). Furthermore, due to the poor intrinsic nucleation activity of Arp2/3, several NPFs for the Arp2/3 complex also localize to and regulate actin polymerization at the AJ (Yamazaki *et al.*, 2007; Kovacs *et al.*, 2011).

In contrast to the Arp2/3 complex, roles at the AJ for members of the formin family of actin nucleators and elongation-promoting factors are less clearly defined. Formins are large (120–200 kDa), multidomain proteins categorized into seven subfamilies comprising 15 members in mammals (Chesarone *et al.*, 2010). Functioning as a dimer, the catalytic formin homology 2 (FH2) domain carries out actin polymerization, acting as a processive barbed-end capper, and the adjacent FH1 domain recruits profilin–G-actin complexes that serve as the substrate for polymerizing linear F-actin filaments (Pruyne *et al.*, 2002; Sagot *et al.*, 2002). Several classes of formins exist in an autoinhibited state via the intramolecular interaction of the C-terminal Diaphanous autoregulatory domain (DAD) with the N-terminal Diaphanous-inhibitory domain (DID; Chesarone *et al.*, 2010). Rho-GTPase signaling and posttranslational modifications, including phosphorylation and myristoylation, are known to regulate the activation and localization of formins (Takeya *et al.*, 2008; Chesarone *et al.*, 2010; Cheng *et al.*, 2011; Kuhn and Geyer, 2014). Furthermore, application of piconewton pulling forces to actin filaments polymerized by Diaphanous-related formin 1 (mDia1) significantly enhances the elongation rate, indicating the mechanosensitive nature of formins (Jegou *et al.*, 2013).

Studies have begun to shed light on roles for formins in polymerizing actin at the AJ to support junctional architecture and function. Studies in mammalian cell culture, *Drosophila*, and mouse models demonstrate a role for mDia1 in augmenting F-actin and E-cadherin at the AJ in a RhoA-dependent manner to preserve epithelial integrity and polarity (Carramusa *et al.*, 2007; Homem and Peifer, 2008; Ryu *et al.*, 2009; Thumkeo *et al.*, 2011). Formin-like 2, a member of the formin-like (FMNL) family, was shown to localize to the AJ in a Rac1-dependent manner in three-dimensional (3D) cultures of Madin–Darby canine kidney cells, in which its depletion resulted in defective lumen formation in 3D spheroids (Grikscheit *et al.*, 2015). Similarly, actin polymerization by a related family member, Fmnl3, was essential at endothelial cell junctions in zebrafish to facilitate proper blood vessel lumenization (Phng *et al.*, 2015). However, the molecular mechanisms underlying the effect of formins on cell–cell adhesion are still poorly understood. Moreover, the role of formins in dynamic multicellular processes such as collective cell migration and wound closure that involve increased tension and turnover at AJ has not been addressed.

Here we identify mDia1 and Fmnl3 as major formins functioning at the AJ in epithelial cells. By measuring the dynamics of E-cadherin and F-actin at the AJ, we show that actin polymerization by these formins decreases the mobility of E-cadherin at AJs, stabilizes the junction, and increases cell–cell adhesion strength. Using small interfering RNA (siRNA)–mediated knockdown, we show that depletion of mDia1 or Fmnl3 also triggers increased protrusive activity and cell spreading, resulting in the loss of lateral junctions. Furthermore, we elucidate a Src kinase and Cdc42–dependent signaling pathway responsible for recruitment and activation of Fmnl3 at the AJ and demonstrate that Fmnl3 recruitment is tension dependent. Finally, we provide evidence that Fmnl3 expression and junctional localization is up-regulated during wound healing to augment AJ and monolayer integrity and facilitate coherent cell sheet migration.

RESULTS

Formin activity affects AJ organization and columnar cell morphology

In polarized Eph4 mammary epithelial monolayers, junctional F-actin and E-cadherin are organized in two distinct forms: a condensed band called the ZA located at the apicalmost portion of the membrane, and sparsely distributed F-actin and E-cadherin along the lateral membranes of contacting cells, termed lateral junctions (Figure 1A). To assess the contribution of formin-dependent actin polymerization to AJ organization, we inhibited endogenous formin activity using the pan-formin small-molecule inhibitor SMIFH2 (Rizvi *et al.*, 2009; Isogai *et al.*, 2015). Here we applied low concentrations of SMIFH2 (20 µM) to minimize cytotoxicity and reduce artifacts induced by Golgi reorganization and loss of p53 transcriptional activity associated with higher doses of SMIFH2 (≥25 µM; Isogai *et al.*, 2015). Suppression of formin activity resulted in several striking phenotypes, including reduction in F-actin and E-cadherin intensity at the AJ, disappearance of lateral junctions, and flattening of cells, resulting in a marked increase in cell-spread area (Figure 1A). Using an automated algorithm for quantification of junctional and cellular parameters on summed intensity *Z*-stack projections, we identified 30 and 21% decreases in fluorescence intensity of F-actin and E-cadherin, respectively, at cell–cell junctions (Figure 1, B and C) as a result of the reduction in lateral junctions. Concurrently, the cell-spread area in SMIFH2-treated monolayers increased significantly in comparison to nontreated monolayers (Figure 1D). Whereas 87% of control cells had an area of ≤800 µm^2, SMIFH2 treatment resulted in 55% of cells with an area of ≥1200 µm^2 (Figure 1D). The increase in cell area was specific to Eph4 monolayers, as formin inhibition in isolated cells did not induce a change in cell spreading (Supplemental Figure S1, A and B). Furthermore, cell spreading was an active process dependent on Arp2/3 complex activity, as double inhibition of formin and Arp2/3 activity, using a mixture of SMIFH2 and CK666 inhibitors, did not result in any change of cell-spread area in treated monolayers (Supplemental Figure S1C).

The loss of lateral junctions after formin inhibition could, in theory, be a direct result of reduced formin activity at the AJ or the indirect consequence of cell spreading. To distinguish between these two possibilities, we plated cells on micropatterned fibronectin islands of defined diameter (100 µm) to limit cell spreading (Figure 1E). We then subjected these islands of cells to SMIFH2 treatment and observed little or no spreading beyond the boundaries of the fibronectin pattern (Figure 1, E and F). Under these conditions, lateral junctions were preserved (Figure 1E), suggesting that loss of lateral junctions is secondary to an active process of cell spreading and loss of typical epithelial columnar cell morphology. Nevertheless, even when cells were forced to remain columnar on the restricting pattern, the SMIFH2-treated islands displayed a small but significant reduction in E-cadherin levels at the AJ (Figure 1G). Taken together, these data suggest a role for F-actin polymerization by formins in stabilizing E-cadherin at the AJ. In addition, inhibition of formin activity triggers Arp2/3-dependent cell spreading, which in turn leads to cell flattening and loss of lateral junctions.

Formin activity is essential for AJ stability

Despite the observed reduction in F-actin and E-cadherin levels at the AJ upon formin inhibition (Figure 1, B and C), Eph4 monolayers remained intact even after 24 h of SMIFH2 treatment. We therefore performed live-cell imaging to examine whether cell–cell junction dynamics was affected by formin inhibition. Short-term imaging (40 min) of E-cadherin–enhanced green fluorescent protein (EGFP) at apical and basolateral planes revealed significant differences

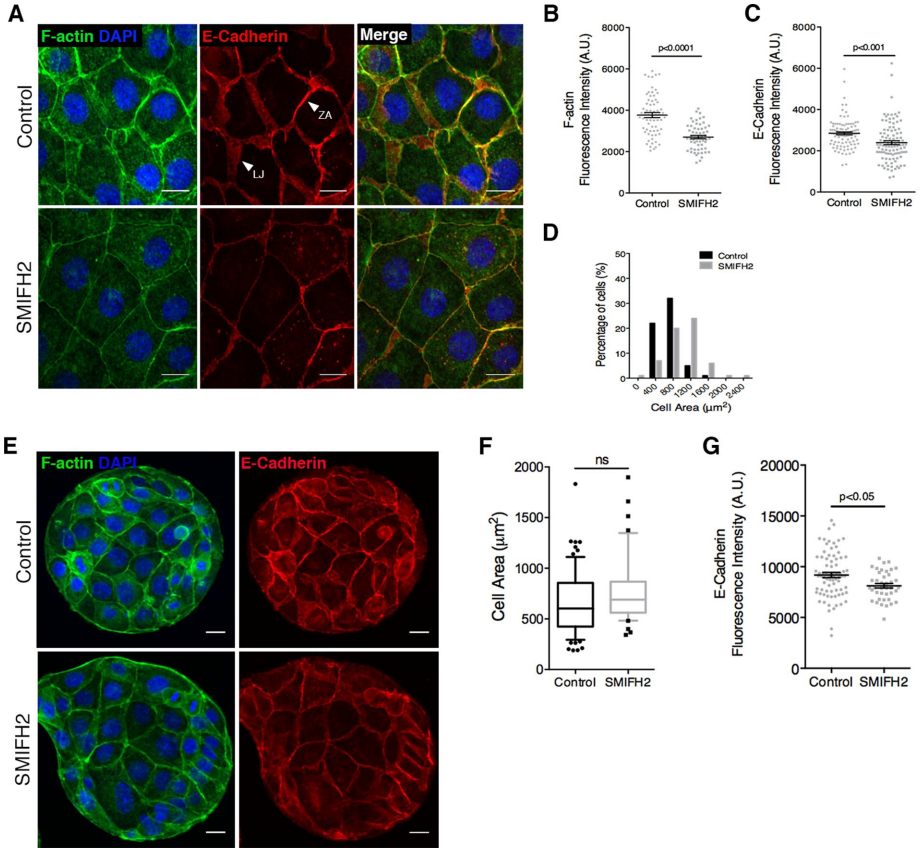

FIGURE 1: Formin-dependent actin polymerization is essential for maintenance of adherens junctions and columnar cell morphology. (A) Representative images of DMSO-treated (Control) and SMIFH2-treated (12 h, here and in subsequent figures, unless specified otherwise) Eph4 monolayers labeled to visualize F-actin and E-cadherin. ZA, zonula adherens; LJ, lateral junction. (B, C) Quantification of F-actin and E-cadherin fluorescence intensity, respectively, at cell–cell junctions for A. Here and in subsequent figures, unless specified otherwise, data are represented for every junction quantified (gray dots) with mean ± SEM; ≥100 junctions from three independent experiments. (D) Frequency histogram of cell area in control and SMIFH2-treated monolayers; 100 cells from three experiments. (E) Representative images of Eph4 islands, with or without SMIFH2 treatment, formed by plating cells on circular fibronectin micropatterns. Area surrounding the islands was nonconducive to cell spreading due to treatment with pluronic acid. (F) Quantification of cell area for E. Box-and-whisker plot; median and 10th–90th percentiles; outliers as individual data points. Ten islands for each condition assessed. (G) Quantification of E-cadherin fluorescence intensity at cell–cell junctions for E. Student's *t* test was used to assess statistical significance in B, C, F, and G. Scale bars, 20 μm (A), 10 μm (E).

between control monolayers and monolayers treated with SMIFH2 for 2 h (Figure 2, A and B). In comparison to the more stable apical ZA in control monolayers, apical junctions in SMIFH2-treated monolayers exhibited greater plasticity and a higher degree of junctional remodeling (either extension or shortening of the junction) during the imaging period (Figure 2A and Supplemental Movie S1). This trend was also reflected in quantitative assessment of the change in junction length over 40 min (Figure 2C) obtained using an algorithm to track the length of junctions at each time point. Analyses of the maximum increase or decrease in junction length during 40 min also revealed a significantly greater variation in SMIFH2-treated monolayers compared with control junctions (Figure 2D). On the basolateral regions of cell–cell contacts, nearly 52% junctions in control monolayers exhibited numerous E-cadherin–containing transient filopodial extensions that originated from and collapsed back into the AJ (Figure 2, B and E, and Supplemental Movie S2). On the other hand, in monolayers pretreated with SMIFH2 before imaging, significantly lower filopodial activity was detected at basolateral junctions (15% junctions); instead, prominent junction-associated lamellipodial protrusions (65% cells) were observed that often terminated at tricellular cell–cell contacts (Figure 2, B and E, and Supplemental Movie S2).

Formins mDia1 and Fmnl3 regulate AJ organization in epithelial cells

To identify specific formins involved in actin regulation and thereby cadherin stability at the AJ, we first used semiquantitative reverse transcription PCR (RT-PCR) analysis to generate a formin expression profile in Eph4 cells for formins belonging to the Diaphanous-related family of formins, namely, Dia, DAAM, FMNL, and FHOD classes. RT-PCR analysis revealed mDia1 as the most abundant formin, followed by formin-like 3 (Fmnl3), and lower expression levels of other formins, including Daam1, Fmnl1/2, and Fhod1/3 (Supplemental Figure S2A). Next we used siRNA-based knockdown (KD) to systematically deplete each of these formins and screened for those that produced phenotypes similar to SMIFH2 treatment (Supplemental Figure S2, B–E). Of interest, KD of the two most abundant formins in Eph4 cells, mDia1 and Fmnl3, recapitulated the phenotype we observed after SMIFH2 treatment (Figure 3A and Supplemental Figure S2, B–E). Furthermore, double KD of both mDia1 and Fmnl3 led to exaggerated defects, resulting in the formation of a sparse monolayer with punctate AJ (Figure 3A). Quantification of junctions in mDia1 KD or Fmnl3 KD monolayers showed 29–31% reduction in F-actin and ~30% reduction in E-cadherin fluorescence intensity at junctions (Figure 3B).

mDia1 was previously shown to regulate F-actin and E-cadherin at the AJ downstream of RhoA (Carramusa *et al.*, 2007; Homem and Peifer, 2008). Antibody staining for endogenous mDia1 revealed diffuse localization in Eph4 cells (Figure 3C, left), whereas Fmnl3 showed prominent enrichment at the AJ (apical and lateral), colocalizing with E-cadherin (Figure 3C, right). It is interesting to note that Fmnl3 labeling could also be detected in the primary cilium (Figure 3C), which warrants further investigation to understand its role in this cellular structure. Consistent with endogenous labeling, GFP-tagged Fmnl3 also localized to the AJ (Figure 3D) and induced a nearly 34% increase in junctional F-actin content in comparison to EGFP mock-transfected cells (Figure 3, D and E). Fmnl3-GFP colocalized with E-cadherin at the AJ, leading to a moderate (27%) but significant enhancement of E-cadherin levels at the AJ (Figure 3, D and F). Although we could not localize mDia1 specifically at the AJ, we tested a role for this formin at cell junctions by expressing an isolated DAD from mDia1 that was previously shown to stimulate endogenous mDia1 (Alberts, 2001; Rao *et al.*, 2013). DAD expression led to a 50% increase in F-actin content

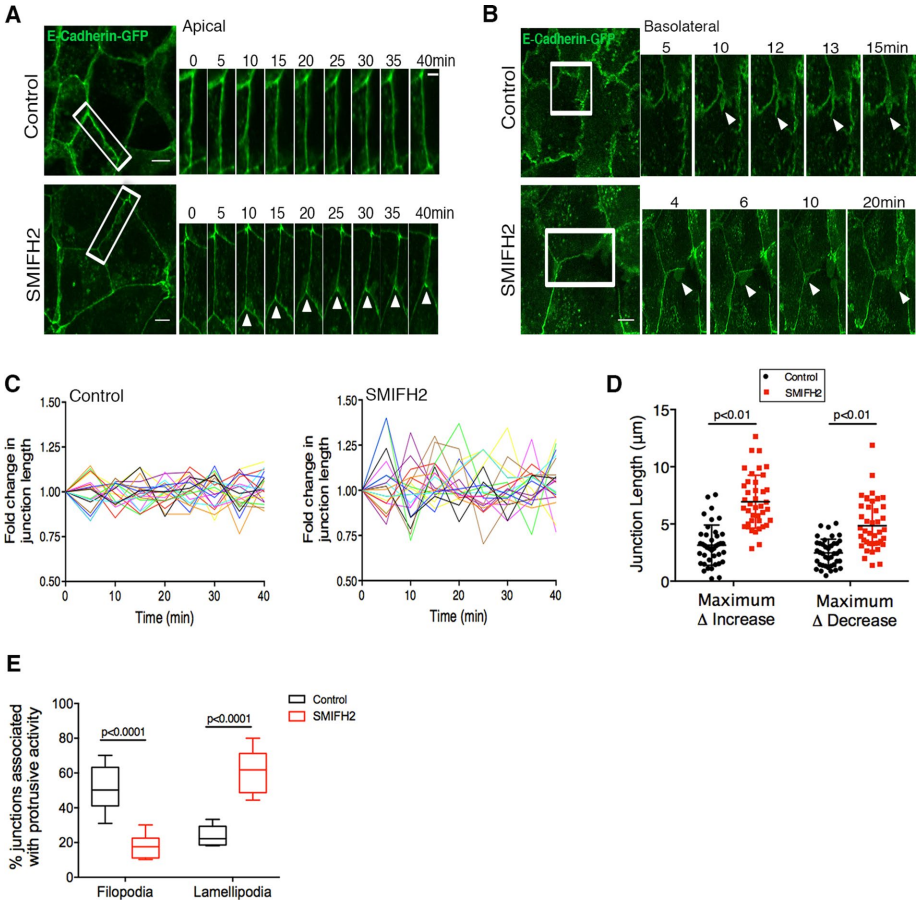

FIGURE 2: Formin activity is essential for AJ stability. (A) Montage of apical ZA (white rectangle) in control and SMIFH2-treated (2 h) monolayers with stable expression of E-cadherin–GFP. Note the stability of ZA in control vs. increased rearrangements of the ZA after SMIFH2 treatment (white arrows, bottom). See Supplemental Movie S1. (B) Montage of E-cadherin-GFP–labeled basolateral cell–cell contacts (white rectangle) in control and SMIFH2-treated (2 h) monolayers. Arrowheads (top) indicate formation of transient filopodia in control vs. lamellipodial protrusions (arrowheads, bottom) after SMIFH2 treatment. See Supplemental Movie S2. (C) Quantification of fold change in junction length over time for apical junctions in control and SMIFH2-treated monolayers. For purpose of visualization, data for 20 junctions are shown here, with each junction represented by a single line. Note the large variation in junctions after SMIFH2 treatment in comparison to control. (D) Quantification of the maximum increase or maximum decrease in apical junction length relative to junction length at the start of imaging for control and SMIFH2 conditions. Data are represented as mean ± SD; >40 junctions from eight movies acquired in two independent experiments. (E) Quantification of junctions associated with filopodial or lamellipodial (%) protrusions at basolateral contacts. Eight movies for each condition; box plot represents minimum to maximum and median. Student's *t* test was used to assess statistical significance in D and E. Scale bars, 10 µm.

of transfected cells compared with EGFP-mock-transfected controls (Figure 3, G and H). Along with the increase in F-actin, DAD-expressing cells also demonstrated elevated levels (33%) of E-cadherin (Figure 3, G and I) at the AJ, suggesting that mDia1, in addition to Fmnl3, contributes to F-actin and E-cadherin organization at the AJ.

To explore the generality of a role for mDia1 and Fmnl3 at the AJ, we also performed KD experiments to deplete these formins in a human mammary epithelial cell line, MCF10A. Indeed, in MCF10A cells, we observed defects in AJ formation and increased cell spreading (Supplemental Figure S3A; KD shown in Supplemental Figure S3, G and H), similar to phenotypes observed in Eph4 cells. Further, immunolabeling to detect endogenous formin localization in MCF10A cells revealed diffuse staining for DIA1 and junctional staining for FMNL3 (Supplemental Figure S3B). Taken together, these data suggest a general role for formins Dia1 and Fmnl3 in regulating AJ organization in epithelial cells.

Formin activity affects molecular dynamics at the AJ

To understand at the molecular level the observed correlation between formin activity and E-cadherin level at AJ, we performed fluorescence recovery after photobleaching (FRAP) experiments on cell–cell junctions in Eph4 monolayers stably expressing GFP-tagged E-cadherin (Figure 4A). From recovery curves obtained for control monolayers, the half-life ($t_{1/2}$) of recovery for E-cadherin was determined to be 151 s, with a mobile fraction of 53 ± 1.43% (Figure 4, B and C). Pretreatment of monolayers with SMIFH2 to inhibit both mDia1 and Fmnl3 before FRAP resulted in an accelerated recovery rate with $t_{1/2}$ = 112 s and increased mobile fraction of 65 ± 2.63% (Figure 4, B and C). Conversely, expression of the DAD to stimulate F-actin polymerization by mDia1 led to significantly slower recovery rates ($t_{1/2}$ = 173 s) and lower mobile fractions (43 ± 1.89%; Figure 4, B and C). Recent FRAP analysis of E-cadherin at cell–cell junctions demonstrated that a significant proportion of E-cadherin molecules were immobilized via specific binding interactions mediated either by the extracellular domain (EC1) and/or interaction with actin via the cytoplasmic domain (Erami *et al.*, 2015). Disruption of *cis* or *trans* interactions in the EC1 domain or actin binding via the cytoplasmic domain of E-cadherin was found to perturb the immobilization of cadherin at the AJ, resulting in increased mobile fractions (Erami *et al.*, 2015). Here we show that modulating F-actin levels also affects the fraction of cadherin immobilized at junctions, highlighting the importance of formin-polymerized F-actin in the stabilization of E-cadherin at the AJ.

Given the distinct localization of Fmnl3 at the AJ, we next focused our efforts on specifically characterizing actin dynamics upon KD or overexpression of Fmnl3 (Figure 4, D–F). The recovery curve for tdTomato-actin at control junctions demonstrated an initial fast recovery phase ($t_{1/2}$ = 19.95 s; Figure 4, E and F), followed by a slower phase that likely represents G-actin incorporation into the F-actin pool. siRNA-mediated depletion of Fmnl3 resulted in acceleration of the initial recovery phase ($t_{1/2}$ = 12.2 s; Figure 4E), suggesting that reduced actin polymerization shifted the G/F-actin balance toward increased G-actin. On the contrary, overexpression of Fmnl3, which increased F-actin content at the AJ (also shown in Figure 3, D and E), resulted in slower recovery of fluorescence at the AJ ($t_{1/2}$ = 25.11 s), correlating with reduced actin turnover and increased F-actin at junctions (Figure 4E). Together these findings indicate a role for formin-mediated actin polymerization in regulating actin turnover at the AJ and in turn affecting cadherin dynamics and mobility at cell–cell junctions.

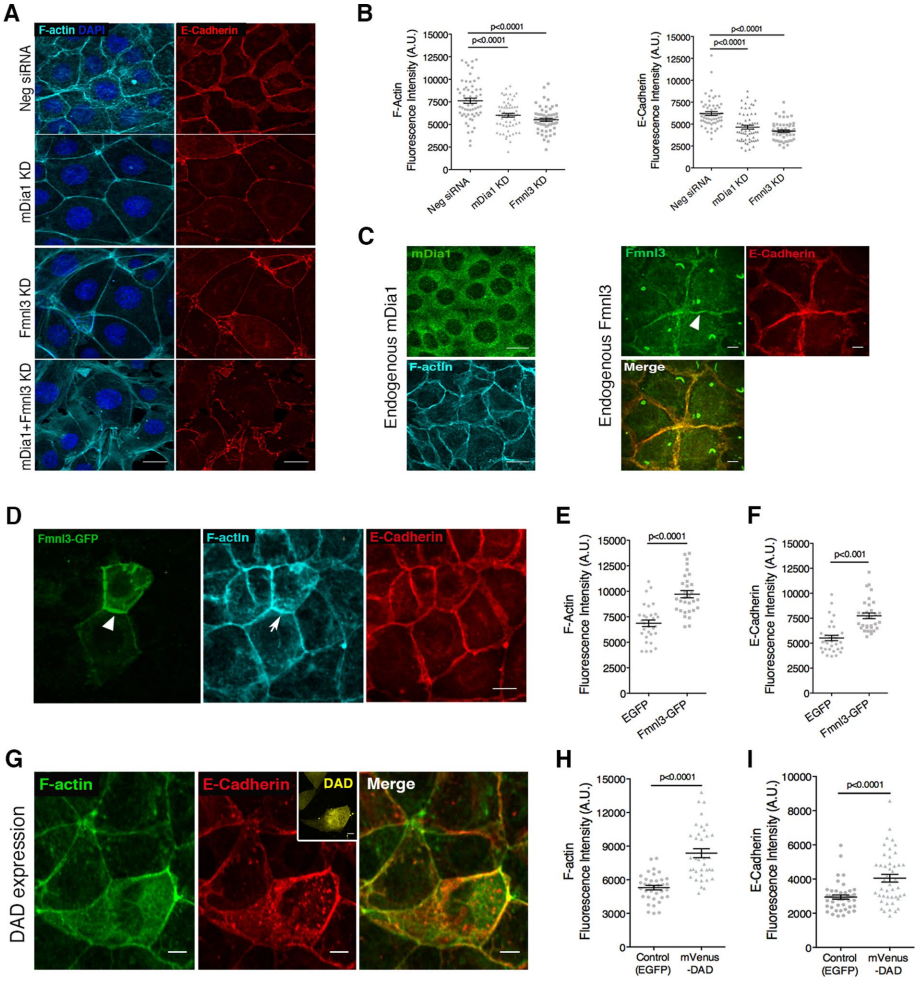

FIGURE 3: Formins mDia1 and Fmnl3 regulate AJ organization in epithelial cells. (A) Phenotypes obtained upon siRNA-mediated KD of mDia1, Fmnl3, or both in Eph4 monolayers, labeled to visualize F-actin and E-cadherin; note the reduction in lateral junctions and increased cell area associated with mDia1 or Fmnl3 KD. (B) Quantification of F-actin and E-cadherin fluorescence intensities at the AJ for A; 65 junctions in control and 62 junctions in mDia1 KD and Fmnl3 KD from three independent experiments, with mean ± SEM (C) Endogenous mDia1 exhibits diffuse localization in Eph4 cells, whereas endogenous Fmnl3 localizes at the AJ, colocalizing with E-cadherin. Arrowhead indicates Fmnl3 labeling at cell–cell junctions. (D) GFP-tagged Fmnl3 localizes to AJ (white arrowhead), resulting in elevated levels of F-actin (white arrow) and E-cadherin. (E, F) Quantification of F-actin and E-cadherin fluorescence intensities, respectively, at the AJ for D; 30 transfected cells per condition from three experiments, with mean ± SEM (G) Representative image of Eph4 cells transfected with mVenus-DAD labeled to visualize F-actin and E-cadherin. Note the abundance of F-actin and E-cadherin in the DAD-transfected cell (mVenus fluorescence shown in inset) in comparison to nontransfected neighbors. (H, I) Quantification of F-actin and E-cadherin fluorescence intensities, respectively, at cell–cell junctions for G; ≥30 transfected cells per condition from thee experiments, with mean ± SEM. Statistical significance assessed using one-way ANOVA in B; Student's *t* test in E, F, H, and I. Scale bars, 20 μm (A, D), 10 μm (C, G).

Movie S4). Closer analysis revealed that cells in Fmnl3 KD monolayers failed to maintain a coherent migrating front, with increased incidence of cell detachment (24.5 ± 2.25% in Fmnl3 KD conditions vs. 4.9 ± 1.23% in control), particularly at the leading edge (Figure 4I and Supplemental Movie S4). Consistently, we also observed the aforementioned phenotypes and associated migration defects in MCF10A subjected to a scratch assay (Supplemental Figure S3, C–E, and Supplemental Movies S5 and S6). Next we investigated the effects on collective migration of silencing both Fmnl3 and mDia1. As illustrated in Figure 3A, combined KD of mDia1 and Fmnl3 in Eph4 cells resulted in the formation of a sparse monolayer, rendering this condition unsuitable for a scratch assay. Hence we chose to introduce siRNAs against these formins on preformed monolayers and subject them to the in vitro scratch assay. Of interest, depletion of both mDia1 and Fmnl3 in Eph4 (Figure 4G, bottom, and Supplemental Movie S7) resulted in complete abrogation of migration (Figure 4, G and H), striking absence of lamellipodium formation at the leading edge, and increased incidence of cytokinesis failure, resulting in numerous rounded cells.

Combining our previous FRAP observations and analyses of collective migration, we hypothesized that weaker cell–cell adhesion was the cause of increased detachment of cells from migrating monolayers. To confirm this, we used a dispase-based dissociation assay (Calautti *et al.*, 1998). In unperturbed monolayers, after treatment with the dispase enzyme, which cleaves the cell–extracellular matrix attachment without affecting cell–cell linkage, only 16.2 ± 2.23% of cells dissociated from the monolayer (Figure 4J). Aggressive perturbation of cell–cell adhesion by ethylene glycol tetraacetic acid (EGTA)–based calcium chelation (Kartenbeck *et al.*, 1982) resulted in 93.2% (±2.4%) of cells being released as single cells into suspension (Figure 4J). Fmnl3 KD before the dispase assay resulted in a dissociation rate of 42.5 ± 3.09% (Figure 4J), which was further exacerbated when combined with mDia1 KD (66.59 ± 3.47%; Figure 4J). This phenomenon was also reproducible in MCF10A cells silenced for FMNL3 expression (Supplemental Figure S3F). Taken together, these results indicate a requirement for Fmnl3 and mDia1 in maintaining adhesion strength at the AJ and sustaining junctional stability during collective migration.

Fmnl3 and mDia1 are essential for monolayer cohesion during collective cell migration

Next we examined the effects of Fmnl3 KD on monolayer dynamics using an in vitro scratch assay to assess collective cell migration. As shown in Figure 4, G and H, all control monolayers (transfected with a nontargeting siRNA) successfully closed the gap within 9–12 h, with cells from both edges migrating coherently and perpendicular to the scratch axis (Figure 4, G and H, and Supplemental Movie S3). In contrast, in Fmnl3 KD monolayers, on average only 62% of the gap was closed after 12 h (Figure 4, G and H, and Supplemental

Src kinase and Cdc42 are upstream activators of formin activity at the AJ

Members of the Diaphanous-related family of formins (Dia, DAAM, FMNL, and FHOD families) are typically autoinhibited through

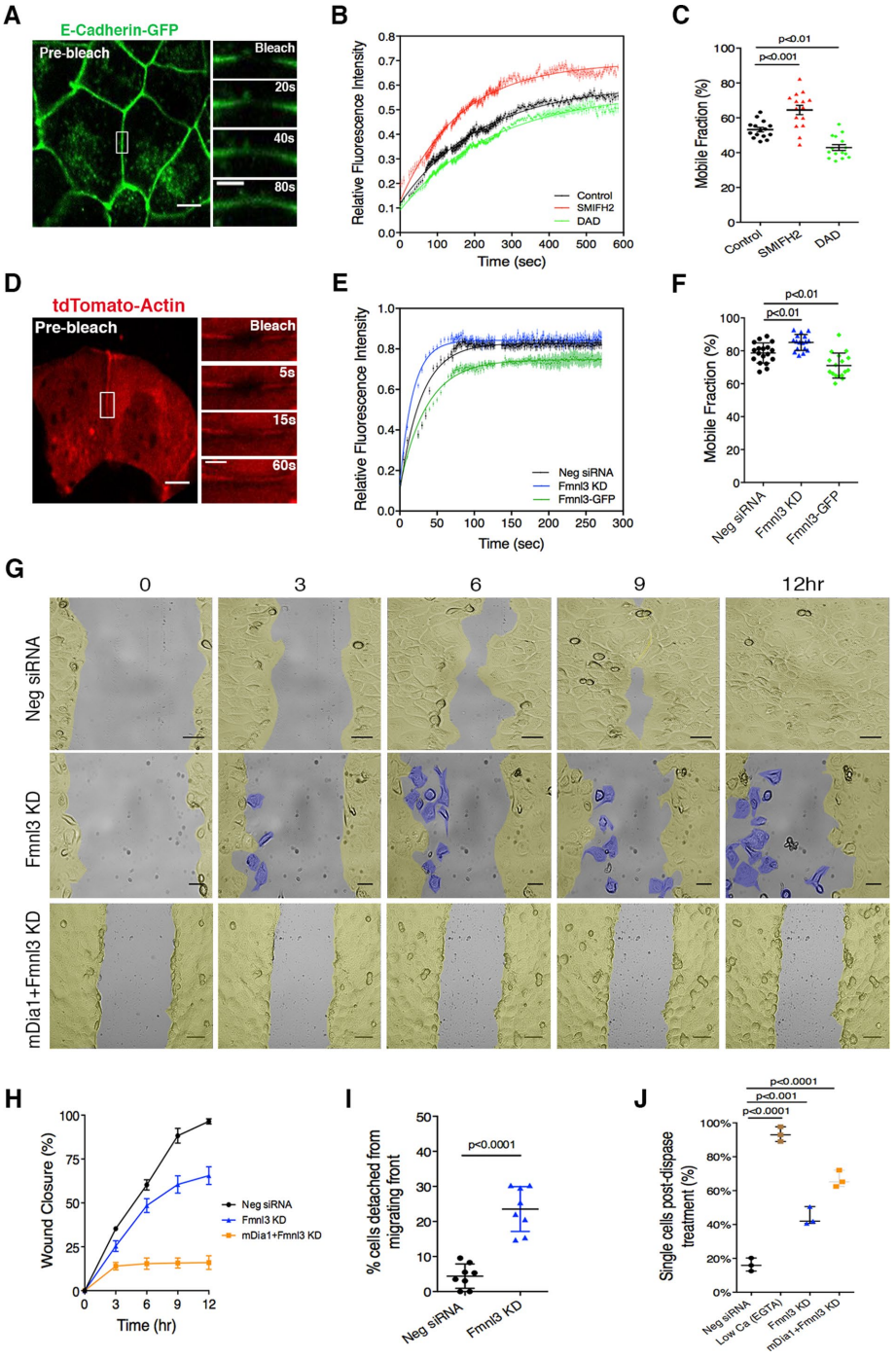

FIGURE 4: Formin activity affects molecular dynamics at the AJ and is essential for monolayer cohesion during collective cell migration. (A) Eph4 monolayer expressing E-cadherin–GFP; junctional E-cadherin–GFP was photobleached (white rectangle) in FRAP experiments. Magnifications illustrate recovery of E-cadherin fluorescence. (B) FRAP recovery curves comparing the effects of SMIFH2 treatment and DAD expression on E-cadherin dynamics at the AJ. Data are shown as an average for 15 junctions tested for each condition. (C) Mobile fractions corresponding to conditions tested in B; 15 junctions for every condition tested, with mean ± SEM. (D) Eph4 cells transfected with tdTomato-actin and plated on fibronectin islands; junctional actin was photobleached (white rectangle) in FRAP experiments. Magnifications illustrate recovery of actin fluorescence. (E) FRAP recovery curves comparing the effects of Fmnl3 KD and Fmnl3 overexpression (Fmnl3-GFP) on actin dynamics at the AJ. Data are shown as an average for 18 junctions tested for Neg siRNA and 17 junctions in Fmnl3 KD and Fmnl3-GFP conditions from three independent experiments. (F) Mobile fractions corresponding to conditions tested in E; 18 (Neg siRNA) or 17 (Fmnl3 KD and Fmnl3-GFP) junctions tested, with mean ± SD. (G) Montage from a movie of an in vitro scratch assay in control (Neg siRNA), Fmnl3 KD, or double KD (mDia1 and Fmnl3) conditions. Images are pseudocolored in yellow to indicate cohesive regions of the cell sheet and in blue (middle) to highlight cells that have detached from the migrating front. See Supplemental Movies S3, S4, and S7. (H) Quantification of wound closure. Eight (Neg siRNA and Fmnl3 KD) and nine (mDia1 + Fmnl3 KD) movies imaged in G, with mean ± SEM. (I) Quantification of cells detaching from migrating front (%). Eight movies for each condition, with mean ± SD. (J) Dispase assay to determine adhesion strength for conditions tested in G. EGTA treatment served as a low–adhesion strength control. Individual dots represent a single experiment ($n = 3$), with mean ± SD. Statistical significance was assessed using one-way ANOVA in C, F, and J; Student's t test in I. Scale bars, 10 μm (A, D), 5 μm (magnification in A, D), 50 μm (G).

an intramolecular interaction between the N-terminal DID and C-terminal DAD (Chesarone *et al.*, 2010). Autoinhibition is released upon binding of an activated Rho-GTPase to the N-terminal GTPase-binding domain (Chesarone *et al.*, 2010). The AJ is a hub for signaling activity involving several classes of Rho-GTPases, as well as serine/threonine and tyrosine kinases (Bertocchi *et al.*, 2012; Zaidel-Bar, 2013).

In an siRNA screen of kinases associated with the AJ (unpublished results), we found that KD of the nonreceptor tyrosine kinase Src resulted in a phenotype similar to mDia1 or Fmnl3 KD, with reduced E-cadherin at the AJ and increased cell spread area. Using the chemical inhibitor of Src (PP2) or siRNA-mediated KD, we confirmed that Src inhibition in Eph4 monolayers leads to loss of lateral junctions and increased cell spreading (Figure 5, A and B, and Supplemental Figure S4A). In addition, Src kinase inhibition also led to weaker cell–cell adhesion strength, as tested via the dispase-based dissociation assay (Figure 5C).

Owing to the similarities in phenotype produced by Src and formin inhibition, we sought to discern whether Src kinase acted upstream of or in parallel with formin activity at the AJ. To this end, we expressed the DAD in Eph4 monolayers and subjected them to Src kinase inhibition (Figure 5D). We found that activation of mDia1 by the exogenous DAD was sufficient to rescue the effects of Src inhibition on E-cadherin levels at AJs and prevent the loss of lateral junctions (Figure 5, D and E). This suggested that formin activation was downstream of Src kinase activity.

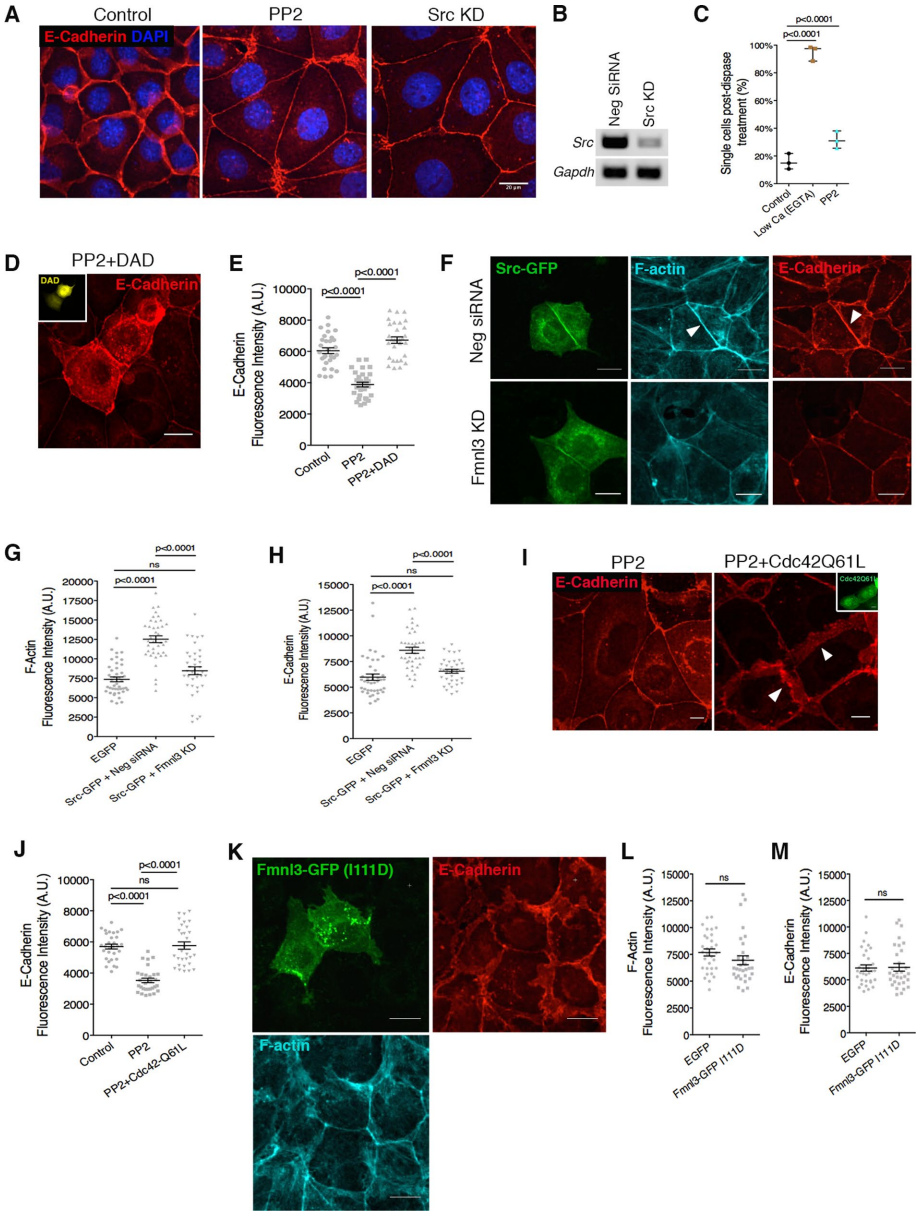

FIGURE 5: Src kinase and Cdc42 are upstream activators of formin activity at the AJ. (A) Src kinase inhibition via PP2 treatment or siRNA-mediated KD phenocopies mDia1 or Fmnl3 KD. (B) PCR analysis for efficiency of Src KD. Glyceraldehyde 3-phosphate dehydrogenase (GAPDH) was used as control. (C) Dispase assay for PP2-treated monolayers. Three independent experiments, with mean ± SD. (D) Activation of endogenous mDia1 via DAD expression (mVenus fluorescence in inset) rescues the Src-inhibition phenotype. Note the dramatic augmentation of the AJ in transfected cells in comparison to nontransfected neighbors. (E) Quantification of E-cadherin fluorescence intensity at the junction for D. Control monolayers were transfected with a GFP vector; ≥30 junctions from transfected cells for each condition from three experiments, with mean ± SEM. (F) Full-length Src-GFP localizes to the AJ, resulting in elevated levels of F-actin and E-cadherin (arrowheads, top). Src-GFP expression combined with Fmnl3 KD abrogates junctional F-actin and E-cadherin augmentation (bottom). (G, H) Quantification of F-actin and E-cadherin fluorescence intensities for F; ≥35 junctions from transfected cells for each condition from three experiments, with mean ± SEM. (I) Expression of constitutively active Cdc42 (GFP shown in inset) rescues the Src-inhibition phenotype. Note the restoration of lateral junctions (white arrowheads) in transfected cells vs. nontransfected neighbors. (J) Quantification of E-cadherin fluorescence intensity for I. Control monolayers were transfected with a GFP vector; ≥ 28 junctions from transfected cells for each condition from three experiments, with mean ± SEM. (K) Fmnl3-GFP (I111D) does not localize to AJ, with no effect on F-actin or E-cadherin. (L, M) Quantification of F-actin and E-cadherin fluorescence intensities for K; ≥26 junctions from transfected cells per condition from three experiments, with mean ± SEM. Statistical significance assessed using one-way ANOVA in C, E, G, H, and J; Student's *t* test in L and M. Scale bars, 20 μm (A, D, F, and K), 10 μm (I).

To further test the role of Src kinase as an upstream regulator of formins, we coexpressed in cells full-length GFP-tagged Src kinase together with a nontargeting control siRNA. As illustrated in Figure 5, F–H, Src-GFP robustly localized at the AJ, with a concomitant increase in F-actin and E-cadherin levels at the junction. Next we cotransfected Src-GFP together with siRNAs targeting Fmnl3. Whereas Src-GFP retained its prominent AJ localization, in this case, we did not observe a significant increase in junctional F-actin or E-cadherin (Figure 5, F–H), suggesting that Fmnl3 is an essential downstream effector of Src kinase at the AJ responsible for the increase in F-actin and E-cadherin.

Previous studies established a role for Src kinase in regulating Rho-GTPase activity at the AJ (Fukuhara *et al.*, 2004). Furthermore, Rho-GTPases are immediate upstream regulators of formin activity. We therefore hypothesized that a Rho-GTPase intermediate existed in the signaling cascade between Src kinase and formin activation. To test this hypothesis, we attempted to rescue the effects of Src kinase inhibition through the expression of constitutive active mutants of the Rho GTPases RhoA, Rac1, and Cdc42. As shown in Figure 5, I and J, expression of constitutively active Cdc42 (Q61L mutation) was sufficient to rescue the phenotype observed with PP2 treatment. Cells expressing active Cdc42 not only had increased E-cadherin levels at the AJ, but also demonstrated the presence of lateral junctions, unlike their nontransfected counterparts (Figure 5, I and J). In contrast, constitutively active mutants of RhoA (V14) or Rac1 (L61) were inadequate to rescue the effects of Src kinase inhibition, with no visible changes in AJ organization detected in comparison to PP2-treated monolayers (Supplemental Figure S4, B and C). These results suggest a role for the Rho-GTPase Cdc42 as a signaling intermediate between Src kinase and formin activation. More recently, Fmnl3 was demonstrated to play a role in filopodia extension during angiogenesis in zebrafish in a Cdc42-dependent manner (Wakayama *et al.*, 2015). Hence we asked whether this was also true at epithelial cell–cell junctions. To test this, we expressed in cells Fmnl3-GFP containing a point mutation (I111D) that abolishes binding to Cdc42 (Wakayama *et al.*, 2015). Close analysis of this mutant revealed no specific cellular localization (Figure 5K) and no qualitative (Figure 5K) or quantitative (Figure 5, L and M) change in F-actin or E-cadherin organization at the AJ, suggesting that Fmnl3 activation and localization at the AJ depended on

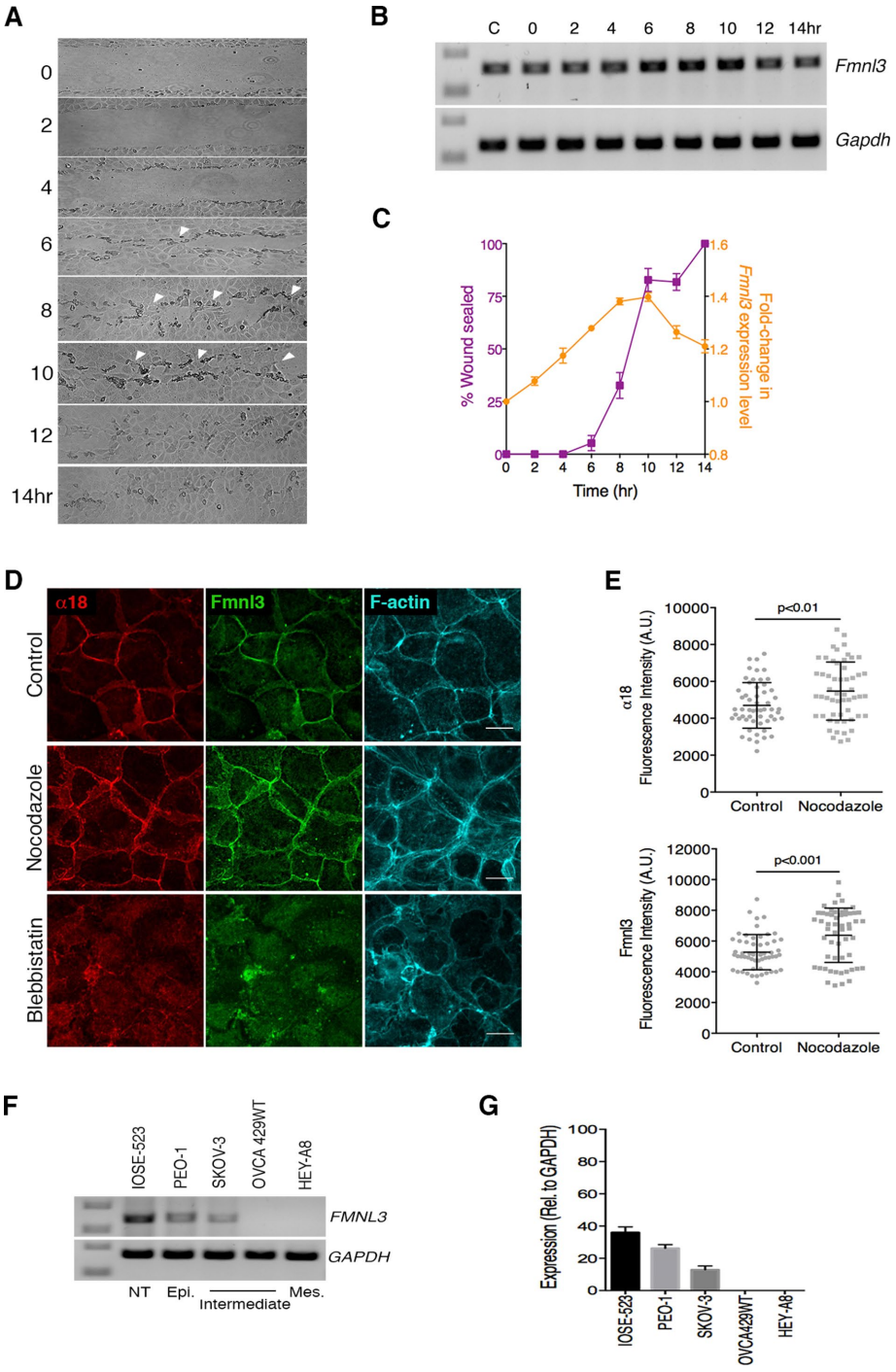

FIGURE 6: Fmnl3 expression is elevated in response to epithelial wounding and is lost in cells that underwent EMT. (A) Time series after wound closure over 14 h (10× magnification). Arrowheads indicate regions where cell fronts establish contact(s) and form de novo AJs. (B) PCR analysis for detection of *Fmnl3* expression levels corresponding to time points illustrated in A. GAPDH was used as a control. Note the increase in intensity of bands, particularly between the 6- and 10-h time points. C, control, unwounded monolayer. (C) Quantification of *Fmnl3* expression level in B, compared with percentage wound sealed at the corresponding time point. Note the increase in *Fmnl3* expression coincident with the phase of active migration. Two independent experiments, with mean ± SEM. (D) Representative images of Eph4 monolayers labeled to visualize α-catenin α18, Fmnl3, and F-actin after treatment with nocodazole or blebbistatin. Note the increased junctional localization of Fmnl3 upon nocodazole treatment (middle) and loss of junctional Fmnl3 after blebbistatin treatment (bottom). (E) Quantification of α18 and Fmnl3 fluorescence intensities at cell–cell junctions for control and nocodazole-treated monolayers in D; >50 junctions from three independent experiments, with mean ± SD. (F) PCR analysis for detection of *FMNL3* expression in human ovarian cancer cell lines. GAPDH was used as a control. NT, nontransformed; Epi., epithelial; Mes., mesenchymal. (G) Quantification of *FMNL3* expression level from F. Two independent experiments, with mean ± SEM. Statistical significance assessed using Student's *t* test in E. Scale bar, 20 μm (D).

Cdc42. Taken together, these results confirm the existence in Eph4 epithelial cells of a Src-Cdc42-Fmnl3 signaling axis that regulates F-actin and E-cadherin at the AJ.

Fmnl3 expression is elevated in response to epithelial wounding and is lost in cells that underwent epithelial–mesenchymal transition

As shown in Figure 3C, Fmnl3 localized to the AJ in nonmigrating monolayers, and its absence led to weak cell–cell adhesion and cell detachment in migrating monolayers (Figure 4, G and J). Therefore we hypothesized that epithelial cells would up-regulate their expression of *Fmnl3* in response to wounding in order to maintain cell–cell junction integrity in the face of increased forces during collective cell migration (Tambe *et al.*, 2011).

To test our hypothesis, we used semiquantitative RT-PCR analysis to assess changes in *Fmnl3* expression concurrent with the time course of migration in an in vitro scratch assay. As shown in Figure 6A, the two migrating fronts generated during the scratch assay began to establish contact within ~6 h. Subsequently, between 8 and 10 h from the start of migration, the migrating fronts established numerous points of contact, and within 12 h, the wound was completely sealed, and long-range collective cell movements ceased. For every time point captured in Figure 6A, we analyzed the mRNA expression level for *Fmnl3*. Of interest, our data revealed gradual but steady up-regulation of *Fmnl3* levels during the course of migration (Figure 6, B and C, and Supplemental Figure S5E), with a peak increase of 1.4-fold between 8 and 10 h, corresponding to the time when the two migrating fronts had established multiple cell–cell contacts. After gap closure was completed between 12 and 14 h, we observed a moderate decrease in *Fmnl3* expression levels.

In addition to changes at the RNA level, we also investigated changes in endogenous Fmnl3 localization in cells that were positioned four or five cell rows behind the scratch edge (Supplemental Figure S5, A and B). In good agreement with the aforementioned expression data, we observed a steady increase in the level of Fmnl3 at cell–cell junctions between 6 and 10 h from the

start of migration. After a nearly twofold increase in Fmnl3 levels at the AJ between 6 and 8 h, we observed a steady reduction at 12 and 14 h when collective migration had halted (Supplemental Figure S5, A and B). These data support the notion that actin polymerization by Fmnl3 is of particular importance during collective cell migration, when cell–cell junctions experience greater forces and require reinforcement of the AJ to support coherent migration as a continuous epithelial sheet.

Next we probed directly whether Fmnl3 recruitment to cell–cell junctions was indeed force sensitive, taking advantage of the α18 antibody, which binds to α-catenin at the AJ in a force-dependent manner (Yonemura *et al.*, 2010). We first confirmed that cell junctions in Eph4 were tension sensitive by exposing monolayers to nocodazole or blebbistatin to increase or decrease cellular contractility, respectively. Consistent with previous studies (Yonemura *et al.*, 2010) and as shown in Supplemental Figure S5, C and D, nocodazole treatment resulted in markedly higher α18 labeling at the AJ, indicating that a higher proportion of α-catenin existed in a stretched conformation. Conversely, reduction of contractility after blebbistatin treatment resulted in near-disassembly of junctions, with little to no detectable α18 or α-catenin labeling at the AJ (Supplemental Figure S5C, bottom). We then compared the localization of α18 and Fmnl3 under similar conditions of increased or decreased contractility. As shown in Figure 6, D and E, recruitment of Fmnl3 at the AJ was significantly enhanced after nocodazole treatment and lost upon blebbistatin treatment. These data further suggest that Fmnl3 is recruited at cell–cell junctions under conditions of increased force application, such as during collective migration.

The phenotype we observed of cell detachment from monolayers upon Fmnl3 KD (Figure 4, G and I) was reminiscent of cells undergoing epithelial-mesenchymal transition (EMT), which often promotes cancer metastasis. Although EMT is a highly complex process, it is commonly associated with loss of cell–cell adhesion and acquisition of mesenchymal features with increased migratory potential (Cannito *et al.*, 2010). Therefore, using semiquantitative RT-PCR analysis, we investigated *FMNL3* expression levels in a range of human ovarian cancer cell lines with nontransformed (IOSE-523), epithelial (PEO-1), mesenchymal (HEY-A8), or intermediate/transitioning phenotypes (SKOV-3 and OVCA429WT; Figure 6F and Supplemental Figure S5F). Our analysis revealed highest expression of *FMNL3* in nontransformed and epithelial ovarian cancer cells (Figure 6, F and G), with no detectable *FMNL3* expression as the cells tended toward more mesenchymal types. Overall these results corroborate a role for Fmnl3 in supporting the epithelial phenotype.

DISCUSSION

Our findings provide evidence of the requirement of formin-dependent actin polymerization in stabilizing E-cadherin at AJs, contributing to cell–cell adhesion strength, preserving columnar cell morphology, and maintaining cohesion during collective migration. Although previous studies identified several formins, including mDia1, FMNL2, and FMNL3, at the AJ (Carramusa *et al.*, 2007; Homem and Peifer, 2008; Gauvin *et al.*, 2015; Grikscheit *et al.*, 2015; Phng *et al.*, 2015), this is the first to show an essential role for formin activity in preventing leader cell dispersion and demonstrate up-regulation of the formin Fmnl3 after epithelial monolayer wounding. Previous studies using wound-healing assays implicated the formin mDia1 in facilitating directed cell migration through its ability to stabilize microtubules in a RhoA-dependent manner (Wen *et al.*, 2004; Goulimari *et al.*, 2005). Although we were unable to specifically localize mDia1 at the AJ or migrating cell fronts in our study, we do not rule out the possibility that the migration defects we observed could also be due to the microtubule-stabilizing property of mDia1.

The identification of Src and Cdc42 as upstream activators of formin activity raises the possibility that formins are mechanoregulated and respond to increased tension at cell–cell and/or cell–matrix adhesions, since both Src and Cdc42 have been shown to be activated in response to mechanical stimulation (Tzima *et al.*, 2003; Wang *et al.*, 2005; Niediek *et al.*, 2012). Indeed, we show here, by varying cellular contractility, that Fmnl3 is recruited to cell–cell adhesions in a force-dependent manner. It is also worth noting that single-molecule tracking studies have demonstrated processive actin polymerization by mDia1 in response to forces applied on cell surfaces (Higashida *et al.*, 2013), further highlighting the mechanosensitive nature of formins. Of interest, in vivo studies in rabbit corneal epithelial wound healing demonstrate an increase in Cdc42 expression correlated with migration, with expression levels tapering off when migration is complete (Pothula *et al.*, 2013), which is highly reminiscent of the trend we observe with Fmnl3. In addition, up-regulation of the actin regulatory protein annexin-2 in a Rho-dependent manner was shown to be crucial for collective migration in intestinal epithelial wound-healing models (Babbin *et al.*, 2007). Hence it is likely that the up-regulation of Rho-GTPases, actin regulators, and actin nucleators, as we demonstrate here, may be a widespread mechanism to regulate actin turnover at cell–cell/cell–matrix adhesions during collective cell migration.

Both literature and proteomic analyses of E-cadherin–based junctions have clearly established the AJ as a focal point of signaling by Rho-GTPases, kinases, and phosphatases (Bertocchi *et al.*, 2012; Zaidel-Bar, 2013; Guo *et al.*, 2014; Van Itallie *et al.*, 2014). Several lines of evidence indicate that cadherin-activated Src kinase signaling positively influences cadherin function at the AJ via various downstream effectors, including phosphoinositide 3-kinase (Pang *et al.*, 2005; McLachlan *et al.*, 2007) and cortactin (Ren *et al.*, 2009). In addition, Src kinase signaling is also known to act upstream of the Rho-GTPase Cdc42 in several cellular contexts, such as establishment of nectin-based cell–cell adhesions (Fukuhara *et al.*, 2004), formation of the cortical actin cap (Kuga *et al.*, 2008), and podosome assembly in endothelial cells (Tatin *et al.*, 2006). Here we describe an additional role for Src kinase at the AJ, which is to support AJ organization and dynamics by promoting the function of Fmnl3 in a Cdc42-dependent manner.

The increase in lamellipodial protrusion and cell spreading we observed upon depletion of mDia1 or Fmnl3 is likely explained by the tilting of balance between Arp2/3 and formin activity, as it was recently demonstrated in both yeast and mammalian cells that the two factors compete for a limited pool of G-actin (Burke *et al.*, 2014; Rotty *et al.*, 2015; Suarez *et al.*, 2015). Lomakin *et al.* (2015) showed that inhibiting myosin-II activity can switch cells from an epithelial to a protrusive, Arp2/3-dependent migratory phenotype, with a key step being the disassembly of the cortical actomyosin bundles found in the ZA of epithelial tissues (Lomakin *et al.*, 2015). Thus it would not be unreasonable to assume that inhibition of formin activity in our system would induce excessive activity of other cellular nucleators (e.g., the Arp2/3 complex) due to the sudden availability of polymerization-competent G-actin in the cell. Hence it is worthwhile to remember in the interpretation of our data that the effects of formin inhibition could be twofold: a direct effect on actin polymerization and E-cadherin stabilization at the AJ, and an indirect effect via stimulation of Arp2/3 complex activity.

Consistent with having an important role in maintaining AJ integrity, we found a correlation between loss of *FMNL3* expression and

EMT in ovarian cancer cells. Whether down-regulation of *FMNL3* is directly involved in EMT will be the subject of future studies. Overall our results identify roles for formins mDia1 and Fmnl3 at cell–cell junctions and delineate a novel Src-Cdc42-Fmnl3 signaling pathway that regulates F-actin and E-cadherin at the epithelial AJ. We demonstrate that this pathway is vital for the maintenance of epithelial cohesion during collective cell migration, making it essential for dynamic processes such as wound repair.

MATERIALS AND METHODS

Cell lines, plasmids, and chemical inhibitors

Eph4 (mouse mammary epithelial origin) was cultured at 37°C and 5% CO_2 atmosphere in DMEM (Invitrogen, Carlsbad, CA) supplemented with 10% fetal bovine serum (FBS; Invitrogen) and 1% penicillin–streptomycin (Invitrogen). Eph4 cells with stable expression of GFP-tagged E-cadherin were kindly shared by Jean-Paul Thiery (Institute of Molecular and Cellular Biology, Singapore) and maintained under similar conditions as wild-type Eph4 cells. MCF10A cultures (human mammary epithelial origin) were maintained at 37°C and 5% CO_2 atmosphere in growth medium composed of DMEM/F12 (Invitrogen) supplemented with 5% horse serum (Invitrogen), 20 ng/ml epidermal growth factor (Peprotech, Rocky Hill, NJ), 0.5 mg/ml hydrocortisone (Sigma-Aldrich, St. Louis, MO), 100 ng/ml cholera toxin (Sigma-Aldrich), 10 µg/ml insulin (Sigma-Aldrich), and 1% penicillin-streptomycin. DMEM/F12 supplemented with 20% horse serum (resuspension medium) was used for trypsinizing and resuspending MCF10A cells during routine passages and sample preparation. Ovarian cancer cell lines of varying phenotypes were obtained from Ruby Huang (Cancer Science Institute, Singapore) and were previously characterized (Huang *et al.*, 2013). IOSE-523, PEO-1, and Hey-A8 were cultured in RPMI 1640 (Invitrogen), and SKOV-3 and OVCA429WT cell lines were grown in DMEM, both supplemented with 10% FBS (without antibiotic).

Plasmid encoding the DAD from formin mDia1 (amino acids 1177–1222) fused C-terminally to an mVenus fluorescent tag (mVenus-DAD) was a gift from Klaus M. Hahn (University of North Carolina, Chapel Hill, NC). Plasmids for expression of GFP-tagged full-length human FMNL3 and FMNL3-I111D were generously shared by Shigetomo Fukuhara (National Cerebral and Cardiovascular Center Research Institute, Osaka, Japan; Wakayama *et al.*, 2015). GFP-c-Src (full-length chicken c-Src cloned into EGFP-N1 vector) and tdTomato-actin (full-length human β-actin cloned into tdTomato-N1 vector) were obtained from the Michael Davidson Collection (Florida State University, Tallahassee, FL; also available from Addgene). Plasmids for expression of RhoA and Cdc42 with the activating mutations V14 and L61, respectively, were provided by Alexander Bershadsky (Mechanobiology Institute, Singapore). Constitutively active yellow fluorescent protein–tagged Rac1 (L61 mutation) was provided by the Lemichez group (C3M University of Nice Sophia Antipolis, Nice, France).

For inhibition of cellular formin activity, confluent Eph4 monolayers were incubated for up to 12 h with 20 µM SMIFH2 (Tocris Biosciences, Bristol, UK), fixed with 4% paraformaldehyde posttreatment, and processed for immunofluorescence staining as described later. Arp2/3 complex or Src kinase inhibition was achieved by incubating confluent monolayers with 100 µM CK666 (Calbiochem, San Diego, CA) or 20 µM PP2 (Sigma-Aldrich), respectively, for 1 h. Nocodazole and blebbistatin treatments were performed for 1 h at concentrations of 10 and 50 µM, respectively. Dimethyl sulfoxide (DMSO) controls were used for all experiments, and CK689 (100 µM/1 h) served as an inactive control for the Arp2/3 complex inhibitor CK666.

Plasmid transfection and siRNA knockdown

All plasmid transfections were performed on Eph4 monolayers plated at 60–70% confluence, using 0.5–1 µg of purified plasmid and Lipofectamine 2000 (Invitrogen) as per the manufacturer's instructions.

Gene silencing experiments were performed by transfecting Eph4 or MCF10A cells with species-specific ON-TARGET plus siRNA oligonucleotides (GE Dharmacon, Lafayette, CO) or a nontargeting siRNA (Neg siRNA; GE Dharmacon) at a final concentration of 50 nM using Lipofectamine 2000 as per the manufacturer's instructions. Cells were fixed and immunolabeled for analysis 24–26 h posttransfection. Concurrently, cell lysates were also prepared from duplicate samples to assess gene knockdown efficiency using semiquantitative PCR analysis. siRNA oligonucleotides used in this study are listed in Supplemental Table S1.

RNA extraction and semiquantitative PCR

Total RNA was extracted from confluent monolayers of cells using TRIzol (Ambion, Carlsbad, CA) as per the manufacturer's instructions. cDNA was synthesized via oligo-dT–primed reverse transcription from 1 µg of total RNA and reagents supplied in the SuperScript III First-Strand Synthesis System for RT-PCR (Invitrogen). Equal volumes of cDNA were then used in a subsequent PCR as template to amplify genes of interest and quantitate expression levels. Gene-specific primers used are listed in Supplemental Table S2. Samples were then analyzed via agarose gel electrophoresis, and images were captured using the ChemidocMP imaging system (Bio-Rad, Hercules, CA) and quantified using the Gel Analyzer plug-in available in ImageJ/Fiji (National Institutes of Health, Bethesda, MD).

Fibronectin patterning

The protocol for stamping circular fibronectin patterns for cell confinement experiments was adapted from Doxzen *et al.* (2013). Briefly, PDMS stamps bearing circular features of 100 µm diameter were prepared using a silanized wafer generated using soft lithography techniques. Stamps were then incubated with a mixture of fibronectin (Sigma-Aldrich) and cyanine 5 (Cy5)-conjugated fibronectin for 1 h, followed by three washes with phosphate-buffered saline (PBS) and air drying. Dried and labeled fibronectin stamps were then gently pressed against a glass-bottom dish (Ibidi, Martinsried, Germany 81151) to replicate the patterns on the dish. The area outside the patterns was then blocked by treatment with 0.2% Pluronic F-127 (Sigma-Aldrich) for 1 h, followed by two washes with PBS before cells were seeded.

In vitro scratch assay

For the in vitro scratch assay, Eph4 or MCF10A cells were plated until confluent on glass-bottom dishes (Iwaki, Newport, UK). The dishes were incubated at 37°C to allow complete cell spreading and formation of a monolayer. Before imaging, a "scratch" was created in the monolayer using a p10 pipette tip. The dishes were rinsed three times with sterile PBS to remove cell debris, imaging medium was added, and cell migration was captured via live-cell imaging as described later (image acquisition was performed for 12–13 h for Eph4 and 24 h for MCF10A).

Dispase-based dissociation assay

Confluent 60-mm dishes of epithelial cells were washed twice in PBS, treated with 2 ml of dispase solution (Life Technologies, Carlsbad, CA), and incubated at 37°C. Samples were monitored using an inverted transmission microscope at 5- to 10-min intervals for ~40–45 min. Postincubation, single cells or clumps of cells

released from each sample were collected and washed twice with PBS. Samples were then centrifuged, resuspended in 500 µl of PBS, and subjected to mechanical disruption by vortexing. The single cells released into suspension were counted using a Countess automated cell counter (Invitrogen). The whole samples were then centrifuged and incubated for 3–4 min at 37°C in TrypLE Express (Life Technologies) to release all cells into suspension. Cell count posttrypsinization was determined as before and used for assay normalization. For a low–adhesion strength control, confluent monolayers were treated with EGTA (4 mM) for 2 h before the dispase assay was performed.

Immunofluorescence and phalloidin staining

Samples for immunofluorescence and/or phalloidin staining were prepared by seeding cells on glass coverslips or 35-mm glass-bottom dishes (Iwaki) in 2 ml of growth medium at a density of 2×10^5 cells/ml, followed by transfection with the plasmids of interest using Lipofectamine 2000 as per the manufacturer's instructions (Invitrogen). Immunofluorescence staining was performed 20–22 h posttransfection. Briefly, cells were fixed by incubation in prewarmed 4% paraformaldehyde for 20 min, followed by permeabilization with 0.2% Triton X-100 for 3 min. Immunostaining was performed at room temperature with the appropriate dilution of desired primary antibody for 1 h, followed by secondary antibody and/or Alexa Fluor–conjugated phalloidin (Life Technologies) for 30 min in dark conditions before mounting of coverslips on glass slides using FluorSave mounting medium (Merck Millipore, Darmstadt, Germany). Primary antibodies used are as follows: E-cadherin (for Eph4 cells, 1:1600, U3254; Sigma-Aldrich), E-cadherin (for MCF10A, 1:100, 610181; BD Biosciences, San Jose, CA), Fmnl3 (1:100, sc-66770; Santa Cruz Biotechnology, Dallas, TX), mDia1 (1:100, 610848; BD Biosciences), α-catenin (1:1000, C2081, Sigma-Aldrich), and α18 (1:200; gift from Shigenobu Yonemura, RIKEN Center for Life Science Technologies, Kobe, Japan). Species-specific secondary antibodies (anti-rat/goat/mouse/rabbit) conjugated to Alexa Fluor 488/568/647 dyes (Life Technologies) were all used at 1:500 dilution, and Alexa Fluor 488/568/647–conjugated phalloidin was used at a dilution of 1:1000.

Image acquisition, live-cell imaging, and FRAP

Images were acquired using a confocal microscope (Ti; Nikon, Tokyo, Japan) fitted with a spinning-disk head (CSU-X1; Yokogawa, Tokyo, Japan), laser launch unit (iLas2; Roper Scientific, Trenton, NJ) and charge-coupled device camera (Evolve Rapid-Cal; Photometrics, Tucson, AZ). A 60×/1.40 numerical aperture (NA) Plan-Apo (Nikon) was used for image acquisition, with *z*-axis movement controlled by a Perfect Focus System (Nikon). MetaMorph software (Molecular Devices, Sunnyvale, CA) was used for image acquisition. Phase-contrast imaging for the in vitro scratch assay was performed with the same microscope setup but at lower magnification using a 20×/0.75 NA Plan-Apo objective (Nikon). All live-cell imaging experiments were carried out in a heated chamber at 37°C and 5% CO_2 atmosphere in DMEM without phenol red, supplemented with 25 mM 4-(2-hydroxyethyl)-1-piperazineethanesulfonic acid (Invitrogen) for Eph4 or in growth medium for MCF10A cells.

FRAP experiments were performed on stable E-cadherin-GFP–expressing Eph4 cells or Eph4 transfected with tdTomato-actin in combination with Fmnl3-GFP or anti-Fmnl3 siRNA. Photobleaching experiments were carried out using the foregoing microscope setup. Prebleach and postbleach (recovery phase) images were acquired using the appropriate laser (20% 491-nm laser power with 100-ms exposure time for E-cadherin–GFP and 15% 561-nm laser with 100-ms exposure for tdTomato-actin). For bleaching, a rectangular region of interest along the junctions (10 μm^2) was bleached using a 405-nm laser pulse at maximum laser power (100%), with an exposure time of 600 (GFP) or 700 ms (tdTomato) for one frame. Images were captured every 1 s for 5 min, followed by every 3 s for an additional 5 min. Data for individual recovery curves were extracted using MetaMorph software and exported to Excel (Microsoft, Redmond, WA) and Prism 6 (GraphPad, La Jolla, CA) for exponential curve fitting. The exponential function used for fitting was $Y = Y_0 + a[1 - \exp(-bx)]$. The values of a and b derived from the exponential curve fit were used to calculate half-time of recovery $t_{1/2} = (\ln 2)/b$ and immobile fraction $F_i = 100[1 - a/(1 - Y_0)]$. Student's t test was then used to verify statistical significance between different experimental groups being assessed.

Image analysis and statistics

Image segmentation and analysis of junctional and cellular parameters were performed using an in-house MATLAB algorithm as follows.

Briefly, the algorithm performs segmentation and analyzes the shape properties of each cell and its junctions using the E-cadherin image, whereas intensity measurement is performed on both E-cadherin and F-actin images. First, each *z*-projected image from the E-cadherin channel is background subtracted and thresholded to generate a binary mask to segment the image into junction region and cell region. Next the junction region is partitioned into junction segments, where each junction segment is the joining boundary of two cell segments. Normal lines are then drawn across every junction segment with a fixed length of 50 pixels. Each normal line, when overlaid on the binary mask, gives us the subset of normal line pixels that belong to the junction segment. The set of intensity values for each junction segment is then obtained by overlaying these pixels on the background-subtracted image. The computation of junction intensity is straightforward by averaging the intensity of all the pixels that belong to each junction segment. The area for each cell segment is estimated from the skeleton image. For analysis of junction lengths from time-lapse movies, a similar algorithm was used that identifies junction segments as the boundaries joining two cell segments. The length of each junction was calculated from the number of pixels of each junction skeleton segment scaled by the pixel size. For each time point, a junction length map was generated and used for tracking length changes over time in Fiji. MATLAB algorithms used in this study for analysis of junctional and cellular parameters are available upon request.

All data generated were exported as Excel files and subsequently to Prism 6 for preparation of graphs and statistical analysis. Quantitative data sets were subjected to Student's t test (for two data sets) or one-way analysis of variance (ANOVA; for more than two data sets) using the statistical functions available in Prism 6. All images were prepared for publication using Photoshop CS6 v13.0 (Adobe Systems).

ACKNOWLEDGMENTS

We are grateful to Shigetomo Fukuhara, Klaus Hahn, and Sasha Bershadsky for sharing plasmids and to Jean-Paul Thiery and Ruby Huang for sharing cell lines. We thank Leyla Kocgozlu and Benoit Ladoux for help with micropatterning and sharing soft lithography wafers and Ong Hui Ting for help with image analysis and writing the MATLAB code. This work was supported by the National Research Foundation Singapore under Fellowship NRF-RF2009-RF001-074 to R.Z.B. and Competitive Research Programme Grant CRP001-084.

REFERENCES

Alberts AS (2001). Identification of a carboxyl-terminal diaphanous-related formin homology protein autoregulatory domain. J Biol Chem 276, 2824–2830.

Babbin BA, Parkos CA, Mandell KJ, Winfree LM, Laur O, Ivanov AI, Nusrat A (2007). Annexin 2 regulates intestinal epithelial cell spreading and wound closure through Rho-related signaling. Am J Pathol 170, 951–966.

Bertocchi C, Vaman Rao M, Zaidel-Bar R (2012). Regulation of adherens junction dynamics by phosphorylation switches. J Signal Transduct 2012, 125295.

Burke TA, Christensen JR, Barone E, Suarez C, Sirotkin V, Kovar DR (2014). Homeostatic actin cytoskeleton networks are regulated by assembly factor competition for monomers. Curr Biol 24, 579–585.

Calautti E, Cabodi S, Stein PL, Hatzfeld M, Kedersha N, Paolo Dotto G (1998). Tyrosine phosphorylation and src family kinases control keratinocyte cell-cell adhesion. J Cell Biol 141, 1449–1465.

Cannito S, Novo E, di Bonzo LV, Busletta C, Colombatto S, Parola M (2010). Epithelial-mesenchymal transition: from molecular mechanisms, redox regulation to implications in human health and disease. Antioxid Redox Signal 12, 1383–1430.

Carramusa L, Ballestrem C, Zilberman Y, Bershadsky AD (2007). Mammalian diaphanous-related formin Dia1 controls the organization of E-cadherin-mediated cell-cell junctions. J Cell Sci 120, 3870–3882.

Cheng L, Zhang J, Ahmad S, Rozier L, Yu H, Deng H, Mao Y (2011). Aurora B regulates formin mDia3 in achieving metaphase chromosome alignment. Dev Cell 20, 342–352.

Chesarone MA, DuPage AG, Goode BL (2010). Unleashing formins to remodel the actin and microtubule cytoskeletons. Nat Rev Mol Cell Biol 11, 62–74.

Collinet C, Lecuit T (2013). Stability and dynamics of cell-cell junctions. Prog Mol Biol Transl Sci 116, 25–47.

Doxzen K, Vedula SR, Leong MC, Hirata H, Gov NS, Kabla AJ, Ladoux B, Lim CT (2013). Guidance of collective cell migration by substrate geometry. Integr Biol (Camb) 5, 1026–1035.

Erami Z, Timpson P, Yao W, Zaidel-Bar R, Anderson KI (2015). There are four dynamically and functionally distinct populations of E-cadherin in cell junctions. Biol Open 4, 1481–1489.

Fukuhara T, Shimizu K, Kawakatsu T, Fukuyama T, Minami Y, Honda T, Hoshino T, Yamada T, Ogita H, Okada M, *et al.* (2004). Activation of Cdc42 by trans interactions of the cell adhesion molecules nectins through c-Src and Cdc42-GEF FRG. J Cell Biol 166, 393–405.

Gauvin TJ, Young LE, Higgs HN (2015). The formin FMNL3 assembles plasma membrane protrusions that participate in cell-cell adhesion. Mol Biol Cell 26, 467–477.

Goulimari P, Kitzing TM, Knieling H, Brandt DT, Offermanns S, Grosse R (2005). Galpha12/13 is essential for directed cell migration and localized Rho-Dia1 function. J Biol Chem 280, 42242–42251.

Grikscheit K, Frank T, Wang Y, Grosse R (2015). Junctional actin assembly is mediated by Formin-like 2 downstream of Rac1. J Cell Biol 209, 367–376.

Guo Z, Neilson LJ, Zhong H, Murray PS, Zanivan S, Zaidel-Bar R (2014). E-cadherin interactome complexity and robustness resolved by quantitative proteomics. Sci Signal 7, rs7.

Harris TJ, Tepass U (2010). Adherens junctions: from molecules to morphogenesis. Nat Rev Mol Cell Biol 11, 502–514.

Harrison OJ, Jin X, Hong S, Bahna F, Ahlsen G, Brasch J, Wu Y, Vendome J, Felsovalyi K, Hampton CM, *et al.* (2011). The extracellular architecture of adherens junctions revealed by crystal structures of type I cadherins. Structure 19, 244–256.

Higashida C, Kiuchi T, Akiba Y, Mizuno H, Maruoka M, Narumiya S, Mizuno K, Watanabe N (2013). F- and G-actin homeostasis regulates mechanosensitive actin nucleation by formins. Nat Cell Biol 15, 395–405.

Homem CC, Peifer M (2008). Diaphanous regulates myosin and adherens junctions to control cell contractility and protrusive behavior during morphogenesis. Development 135, 1005–1018.

Hong S, Troyanovsky RB, Troyanovsky SM (2013). Binding to F-actin guides cadherin cluster assembly, stability, and movement. J Cell Biol 201, 131–143.

Huang RY, Wong MK, Tan TZ, Kuay KT, Ng AH, Chung VY, Chu YS, Matsumura N, Lai HC, Lee YF, *et al.* (2013). An EMT spectrum defines an anoikis-resistant and spheroidogenic intermediate mesenchymal state that is sensitive to e-cadherin restoration by a src-kinase inhibitor, saracatinib (AZD0530). Cell Death Dis 4, e915.

Isogai T, van der Kammen R, Innocenti M (2015). SMIFH2 has effects on Formins and p53 that perturb the cell cytoskeleton. Sci Rep 5, 9802.

Jegou A, Carlier MF, Romet-Lemonne G (2013). Formin mDia1 senses and generates mechanical forces on actin filaments. Nat Commun 4, 1883.

Kartenbeck J, Schmid E, Franke WW, Geiger B (1982). Different modes of internalization of proteins associated with adhaerens junctions and desmosomes: experimental separation of lateral contacts induces endocytosis of desmosomal plaque material. EMBO J 1, 725–732.

Kovacs EM, Verma S, Ali RG, Ratheesh A, Hamilton NA, Akhmanova A, Yap AS (2011). N-WASP regulates the epithelial junctional actin cytoskeleton through a non-canonical post-nucleation pathway. Nat Cell Biol 13, 934–943.

Kuga T, Hoshino M, Nakayama Y, Kasahara K, Ikeda K, Obata Y, Takahashi A, Higashiyama Y, Fukumoto Y, Yamaguchi N (2008). Role of Src-family kinases in formation of the cortical actin cap at the dorsal cell surface. Exp Cell Res 314, 2040–2054.

Kuhn S, Geyer M (2014). Formins as effector proteins of Rho GTPases. Small GTPases 5, e29513.

Lomakin AJ, Lee KC, Han SJ, Bui DA, Davidson M, Mogilner A, Danuser G (2015). Competition for actin between two distinct F-actin networks defines a bistable switch for cell polarization. Nat Cell Biol, 17, 1435–1445.

McLachlan RW, Kraemer A, Helwani FM, Kovacs EM, Yap AS (2007). E-cadherin adhesion activates c-Src signaling at cell-cell contacts. Mol Biol Cell 18, 3214–3223.

Niediek V, Born S, Hampe N, Kirchgessner N, Merkel R, Hoffmann B (2012). Cyclic stretch induces reorientation of cells in a Src family kinase- and p130Cas-dependent manner. Eur J Cell Biol 91, 118–128.

Pang JH, Kraemer A, Stehbens SJ, Frame MC, Yap AS (2005). Recruitment of phosphoinositide 3-kinase defines a positive contribution of tyrosine kinase signaling to E-cadherin function. J Biol Chem 280, 3043–3050.

Phng LK, Gebala V, Bentley K, Philippides A, Wacker A, Mathivet T, Sauteur L, Stanchi F, Belting HG, Affolter M, *et al.* (2015). Formin-mediated actin polymerization at endothelial junctions is required for vessel lumen formation and stabilization. Dev Cell 32, 123–132.

Pothula S, Bazan HE, Chandrasekher G (2013). Regulation of Cdc42 expression and signaling is critical for promoting corneal epithelial wound healing. Invest Ophthalmol Vis Sci 54, 5343–5352.

Pruyne D, Evangelista M, Yang C, Bi E, Zigmond S, Bretscher A, Boone C (2002). Role of formins in actin assembly: nucleation and barbed-end association. Science 297, 612–615.

Rao MV, Chu PH, Hahn KM, Zaidel-Bar R (2013). An optogenetic tool for the activation of endogenous diaphanous-related formins induces thickening of stress fibers without an increase in contractility. Cytoskeleton 70, 394–407.

Ren G, Helwani FM, Verma S, McLachlan RW, Weed SA, Yap AS (2009). Cortactin is a functional target of E-cadherin-activated Src family kinases in MCF7 epithelial monolayers. J Biol Chem 284, 18913–18922.

Rizvi SA, Neidt EM, Cui J, Feiger Z, Skau CT, Gardel ML, Kozmin SA, Kovar DR (2009). Identification and characterization of a small molecule inhibitor of formin-mediated actin assembly. Chem Biol 16, 1158–1168.

Rotty JD, Wu C, Haynes EM, Suarez C, Winkelman JD, Johnson HE, Haugh JM, Kovar DR, Bear JE (2015). Profilin-1 serves as a gatekeeper for actin assembly by Arp2/3-dependent and -independent pathways. Dev Cell 32, 54–67.

Ryu JR, Echarri A, Li R, Pendergast AM (2009). Regulation of cell-cell adhesion by Abi/Diaphanous complexes. Mol Cell Biol 29, 1735–1748.

Sagot I, Rodal AA, Moseley J, Goode BL, Pellman D (2002). An actin nucleation mechanism mediated by Bni1 and profilin. Nat Cell Biol 4, 626–631.

Suarez C, Carroll RT, Burke TA, Christensen JR, Bestul AJ, Sees JA, James ML, Sirotkin V, Kovar DR (2015). Profilin regulates F-actin network homeostasis by favoring formin over Arp2/3 complex. Dev Cell 32, 43–53.

Takeichi M (2014). Dynamic contacts: rearranging adherens junctions to drive epithelial remodelling. Nat Rev Mol Cell Biol 15, 397–410.

Takeya R, Taniguchi K, Narumiya S, Sumimoto H (2008). The mammalian formin FHOD1 is activated through phosphorylation by ROCK and mediates thrombin-induced stress fibre formation in endothelial cells. EMBO J 27, 618–628.

Tambe DT, Hardin CC, Angelini TE, Rajendran K, Park CY, Serra-Picamal X, Zhou EH, Zaman MH, Butler JP, Weitz DA, *et al.* (2011). Collective cell guidance by cooperative intercellular forces. Nat Mater 10, 469–475.

Tatin F, Varon C, Genot E, Moreau V (2006). A signalling cascade involving PKC, Src and Cdc42 regulates podosome assembly in cultured endothelial cells in response to phorbol ester. J Cell Sci 119, 769–781.

Thumkeo D, Shinohara R, Watanabe K, Takebayashi H, Toyoda Y, Tohyama K, Ishizaki T, Furuyashiki T, Narumiya S (2011). Deficiency of mDia, an actin nucleator, disrupts integrity of neuroepithelium and causes periventricular dysplasia. PLoS One 6, e25465.

Tzima E, Kiosses WB, del Pozo MA, Schwartz MA (2003). Localized cdc42 activation, detected using a novel assay, mediates microtubule organizing center positioning in endothelial cells in response to fluid shear stress. J Biol Chem 278, 31020–31023.

Van Itallie CM, Tietgens AJ, Aponte A, Fredriksson K, Fanning AS, Gucek M, Anderson JM (2014). Biotin ligase tagging identifies proteins proximal to E-cadherin, including lipoma preferred partner, a regulator of epithelial cell-cell and cell-substrate adhesion. J Cell Sci 127, 885–895.

van Roy F, Berx G (2008). The cell-cell adhesion molecule E-cadherin. Cell Mol Life Sci 65, 3756–3788.

Verma S, Han SP, Michael M, Gomez GA, Yang Z, Teasdale RD, Ratheesh A, Kovacs EM, Ali RG, Yap AS (2012). A WAVE2-Arp2/3 actin nucleator apparatus supports junctional tension at the epithelial zonula adherens. Mol Biol Cell 23, 4601–4610.

Verma S, Shewan AM, Scott JA, Helwani FM, den Elzen NR, Miki H, Takenawa T, Yap AS (2004). Arp2/3 activity is necessary for efficient formation of E-cadherin adhesive contacts. J Biol Chem 279, 34062–34070.

Wakayama Y, Fukuhara S, Ando K, Matsuda M, Mochizuki N (2015). Cdc42 mediates Bmp-induced sprouting angiogenesis through Fmnl3-driven assembly of endothelial filopodia in zebrafish. Dev Cell 32, 109–122.

Wang Y, Botvinick EL, Zhao Y, Berns MW, Usami S, Tsien RY, Chien S (2005). Visualizing the mechanical activation of Src. Nature 434, 1040–1045.

Wen Y, Eng CH, Schmoranzer J, Cabrera-Poch N, Morris EJ, Chen M, Wallar BJ, Alberts AS, Gundersen GG (2004). EB1 and APC bind to mDia to stabilize microtubules downstream of Rho and promote cell migration. Nat Cell Biol 6, 820–830.

Wu SK, Gomez GA, Michael M, Verma S, Cox HL, Lefevre JG, Parton RG, Hamilton NA, Neufeld Z, Yap AS (2014). Cortical F-actin stabilization generates apical-lateral patterns of junctional contractility that integrate cells into epithelia. Nat Cell Biol 16, 167–178.

Wu Y, Kanchanawong P, Zaidel-Bar R (2015). Actin-delimited adhesion-independent clustering of E-cadherin forms the nanoscale building blocks of adherens junctions. Dev Cell 32, 139–154.

Yamazaki D, Oikawa T, Takenawa T (2007). Rac-WAVE-mediated actin reorganization is required for organization and maintenance of cell-cell adhesion. J Cell Sci 120, 86–100.

Yonemura S, Wada Y, Watanabe T, Nagafuchi A, Shibata M (2010). alpha-Catenin as a tension transducer that induces adherens junction development. Nat Cell Biol 12, 533–542.

Zaidel-Bar R (2013). Cadherin adhesome at a glance. J Cell Sci 126, 373–378.